Flow Structure in the Gap between Two Bluff Bodies

Diego Arcas[*] and Fred. Browand.[†]
University of Southern California, Los Angeles, California, 90089-1191

Mustapha Hammache[‡]
University of Southern California, Los Angeles, California, 90089-1191

The flow in the gap between two bluff bodies that together resemble a model tractor-trailer is investigated using Particle Image Velocimetry (PIV). The velocity field in the gap is experimentally observed to persist for periods of time in an essentially symmetric state or in an asymmetric state. A classification of velocity fields based on a Proper Orthogonal Decomposition (POD) of the flow is performed and the two most energetic basic states are shown to be these same symmetric and asymmetric states. As the flow moves between symmetric and asymmetric conditions, the contribution of the various eigenmodes is demonstrated. Flow states in the symmetric condition can be further subdivided into those *transitional* states which mark a movement of the flow between asymmetries and those symmetric *steady* states in which the flow may rest for longer periods of time.
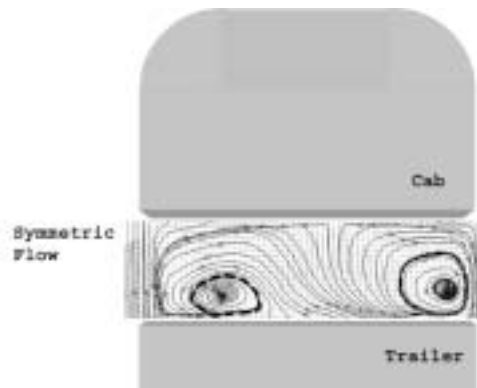
I.   Introduction

THE study of the flow in the gap formed between two bluff bodies has previously been investigated with regards to its influence on aerodynamic drag of the two-body system. Koenig[4] investigated a tandem combination of an axisymmetric cylinder placed behind a circular plate, and reported dramatic changes in the overall drag force of the two-body combination when the separation distance and the ratio of azimuthal radii of the trailing cylinder to the leading plate were varied. They showed that a sharp decrease in drag was related to the smooth r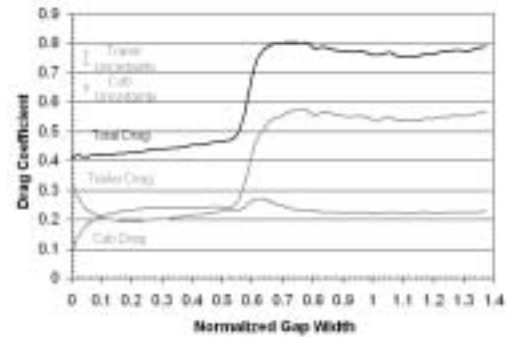eattachment of the flow from the circular plate to the nose of the cylinder. Koenig[4] did not provide a detailed description of the flow in the gap between the two bodies.

Figure 1. Variation of drag coefficient with gap spacing for the trailer, tractor, and total .

Figure 2. Time-averaged streamline patterns of the flow in the gap at zero yaw, G/√A=0.28.

The problem of gap flow has received renewed attention as the need to design more aerodynamically efficient heavy road vehicles has enkindled a plethora of aerodynamic studies focused on different aspects of the truck-trailer tandem geometry. A key feature of this geometry is undoubtedly the gap formed between the cab and the truck. The behavior in this region is central not only in as much as it accounts for a substantial contribution to the overall drag of the vehicle, but also because it is a factor in the determination of the lateral stability properties. This paper presents a classification of the

---

[*] Ph.D. Student, Aerospace and Mechanical Engineering, Los Angeles, CA-90089/1191.
[†] Professor, Aerospace and Mechanical Engineering, Los Angeles, CA-90089/1191.
[‡] Research Assistant Professor, Aerospace and Mechanical Engineering, Los Angeles, CA-90089/1191.
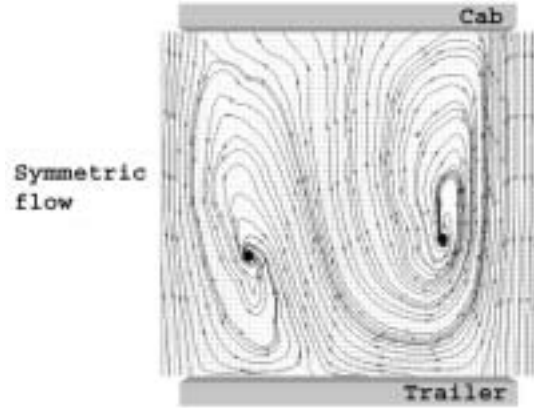
flow behavior in the gap between two isolated bluff bodies with application to heavy road vehicles. The state of the flow is based upon a topological approach in which the various flow states are identified as linear combinations of orthogonal "coherent structures" obtained by performing a Proper Orthogonal Decomposition (POD) of the velocity field in the gap.

Recent wind tunnel studies by Hammache[3] of the aerodynamic drag of a simplified model tractor-trailer reveal a substantial rise in the total drag of the tandem as the distance between tractor and trailer increases. Their result is shown in Fig. 1.
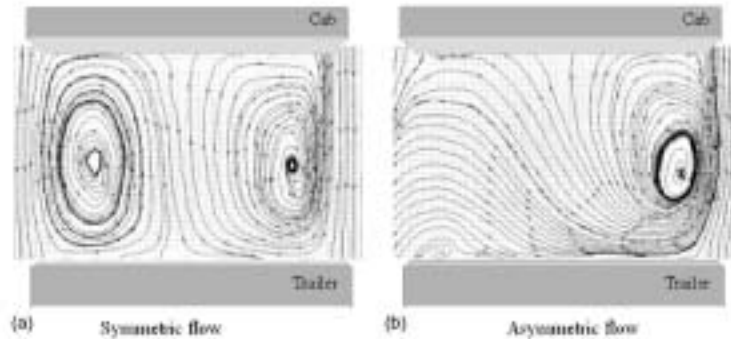
The critical gap for the drag rise comes near the value $G/\sqrt{A}=0.5$, where G is the gap spacing and (A, the square root of the truck frontal area), is the scaling parameter. For gap spacing below the critical gap the drag is low and the flow consists of a nearly symmetric, donut-shaped eddy within the gap. A horizontal slice through the mid-plane would reveal the recirculating eddy-flow as in Fig. 2, for the value $G/\sqrt{A}=0.28$.

Figure 3. Time-averaged streamline patterns of the flow in the gap at zero yaw, $G/\sqrt{A}=1.0$.

Beyond the drag rise at $G/\sqrt{A}==0.7$, the drag falls slightly, but remains high. In this regime, the gap flow has a wake-like character. That is, the mean streamlines from the cab close near the nose of the trailer, and the flow wanders from side to side as vorticity is alternately shed from the gap region, Fig. 3.

The regime $G/\sqrt{A}=0.5$-0.7 is much more interesting. The flow, at times, consists of the nearly symmetric, donut-shaped eddy within the gap, as would appear at shorter gaps, Fig. 4(a).

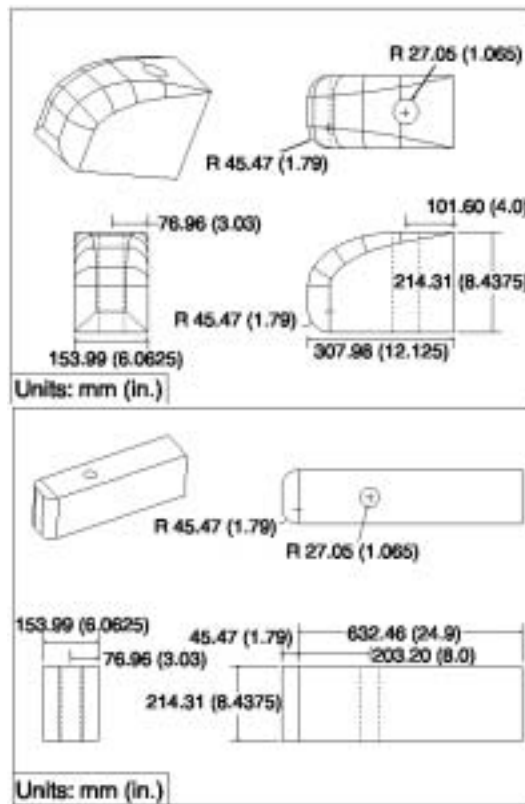**Figure 4. Velocity field in the mid-plane, $G/\sqrt{A}=0.65$. (a) symmetric, (b) asymmetric states.**

At other times the flow is strongly asymmetric across the gap, as in Fig. 4(b). Flow enters the gap on one side, and most of this flow crosses the gap and exits on the opposite side. The mean cross-flow in the gap can be as large as 30% of the free stream velocity. Since the cab and trailer are aligned with the flow, the cross-gap flow changes direction in an unpredictable manner. Because it is not possible to achieve perfect alignment, one side or the other is slightly favored, as will be discussed later. The main objective of this paper is to characterize the flow behavior above the critical gap length on the basis of the structural features revealed by a Proper Orthogonal Decomposition of the data set. The supercritical gap $G/\sqrt{A}=0.72$ was chosen for analysis.

II. Experimental Set-up

A. The Flow Facility

Experiments were conducted in the Dryden wind tunnel at USC. The test section is octagonal in cross section; the sides of the octagon are 1.37 m, apart. For the purpose of ground vehicle studies, a ground-plane has been placed in the wind tunnel such that 5 sides of the octagon lie above the plane. The ground-plane is actually a shallow box
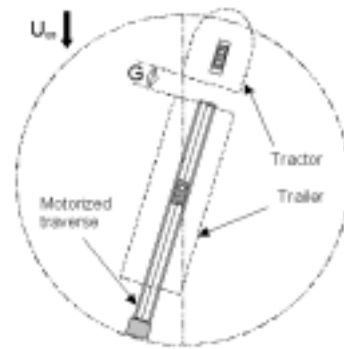
that spans the width of the wind tunnel (1.37 m), and is approximately 5.8 m in length. The ground-plane box houses a stepper-motor-controlled traverse that opens and closes the gap by moving the model trailer in the downstream direction. The position of the tractor, or cab, is fixed. Both tractor and trailer rest on the surface of an interior turntable of diameter 1.22 m to allow the model to be yawed with respect to the flow direction, as shown in Fig. 5. The ground-plane box is mounted in the wind tunnel at a very slight positive angle of attack (one degree) to compensate for boundary layer growth on the walls. The front edge of the ground plane box is a 3:1 ellipse to avoid leading-edge separation. To control boundary layer growth the surface of the ground-plane consists of a sandwich of punched plates-the smallest holes, 1mm in diameter on 4 mm centers, are in the topmost plate. Slight suction is applied to the plenum below the porous top surface to remove the boundary layer fluid. The displacement thickness of the turbulent boundary layer is less than 1 mm over the forward three meters of the

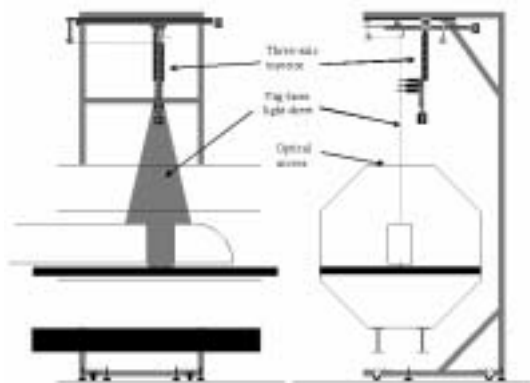**Figure 5. Detail of turntable and traverse mechanism inside ground plane.**

plate surface. The pressure gradient, dCp/dx -measured along the wind tunnel ceiling-is approximately zero (0.003/m) when the tunnel is operated without the truck model.

The measurements are performed at wind tunnel speeds between 24-28 m/s. The model Reynolds number for the tests, based upon the square root of the truck cross-sectional area, (A=0.181 m2), is about 340,000 at the free stream speed, U = 28 m/s. The turbulence level at these speeds is less than 0.25 % in the bandwidth above 1/10 Hz which contains all the measurable fluctuation.

B. Details of the simplified truck models

A bluff-body model representing a simplified model of a tractor and trailer, Fig. 6, is milled from high-density Spyder-foam on a small CNC machine. The use of a Spyder-foam allows for rapid prototyping, whereby the shape can be modified quickly and accurately. The model is roughly 1/15-scale, with no linkage between the simplified tractor, or cab, and trailer. The radius of curvature of the vertical leading edges on the cab is determined by the desire to maintain attached flow. This requires a Reynolds number based upon the edge radius of approximately 70,000, and for wind tunnel speeds in excess of 24 m/s, results in an edge radius of 4.55 cm (Cooper[1], Hammache[3]).

The model cab and trailer are each supported above the ground plane a distance 4.37 cm (=0.28 x W, trailer width). The circular holes in the model cab and trailer each house a 6-component force balance (AMTI, Watertown, MA). The balance and supporting structure is made flush with the flat underside of the model. Two slender posts of diameter 6.35 mm extend through a slot in the ground-plane to connect cab and trailer separately to supports contained within the ground plane box (Fig. 5).

Figure 6. Schematics of tractor and trailer with dimensions.

C. Flow-field images

Conventional two-component digital particle image velocimetry (DPIV) is applied to the gap region between the cab and trailer, as schematically indicated in Fig. 7. Laser light (Spectrum Physics, 450 nm, pulse duration 5 ns, 200 mJ/pulse) is spread into a horizontal (shown vertical, in Fig. 7) sheet of the order of 1-2mm in thickness, and

Figure 7. Schematic of laser illuminated area of the flow (laser sheet is shown vertically for clarity).

introduced through a glass window at one side of the test section. The camera (Kodak EP 202, 1 Mpixel) is positioned above the test section. To interrogate horizontal planes at different heights, the camera and light sheet move in concert under stepper motor control so that magnification and field-of-view remain constant. Here, the field of view is approximately 250 mm square.

Vapor droplets are seeded into the flow using a commercial Colt droplet generator. The formula mixture supplied by the manufacturer is first vaporized, and then allowed to condense into droplets of the order of 1 micron in size. They readily pass through the screens in the wind tunnel settling chamber. Droplets are introduced upstream and allowed to pass several times around the wind tunnel circuit. After several passages, the mixture evaporates and must be replenished. Even after several years of operation, we have noticed little or no residue build-up on the screens or on the interior walls of the wind tunnel.

The DPIV technique requires two images separated by a short time interval. The time interval between images is sufficient to allow the droplets to travel no more than about 5 pixels-in the present case the interval is approximately 50 microseconds. The images are interrogated locally by computing the value of the image cross-correlation within a sub-domain labeled Sample A-Sample B in Fig. 8.
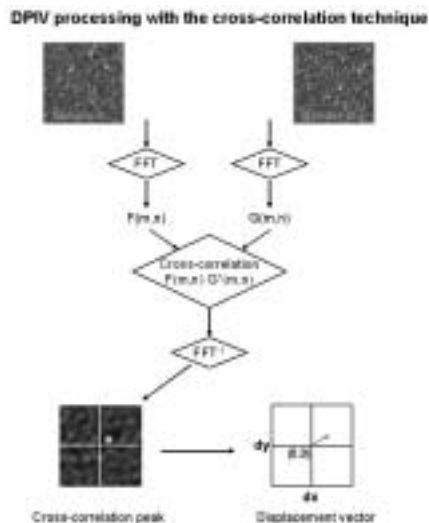
The local cross-correlation between images is often computed in Fourier space as depicted in Fig. 8, although this mathematical operation imposes restrictions that are not necessary nor always desirable[3]. Local cross-correlation yields a local displacement vector, and repeating the process throughout the image yields a displacement vector field. Knowing the precise time interval between image pairs converts the displacement field into a velocity field.

The sub-domain size, or the size of the region over which the flow field is averaged, is about 32x32 pixels. Each sub-domain is overlapped by one-half, yielding a spatial resolution of approximately 16 pixels, or about 4 mm in physical space. At this scale, the measurements do not adequately resolve flow near walls, such as the details of the boundary layer structure on the rear of the cab or the front of the trailer. The resultant vector field within the gap contains approximately 60x60 vectors (3600 vectors total).

The gap flow-field is sampled at a gap spacing of 0.72, and 0° yaw. Images are recorded in bursts of 50 images at the limiting repetition rate of 10 images per second (laser limit). The convection time for flow past the model is less than 0.04 seconds, but the flow can remain in a "state" for a period of several seconds, so the 50-image bursts are spaced over several minutes to insure proper sampling weights for the realizations. Seven such bursts are acquired for a total of 350 image pairs.

Figure 8. Schematic of the method of data acquisition and processing using DPIV.

D. POD Method

The Proper Orthogonal Decomposition (POD) is a powerful data analysis method also known as the Kharunen-Loeve decomposition. It has been extensively used in fields such as image processing and pattern recognition, and it was first introduced to the fluid dynamics community by Lumley[5]. It allows for the extraction of a basis set of

experimental eigenfunctions. It is presumed that the basis eigenfunctions have physical significance and somehow represent the organized structures present in the data set.

POD analysis yields a complete set of orthogonal functions in the sense that:

$$\left(\Phi_i, \Phi_j\right) = \int_L \Phi_i(\vec{x}) \times \Phi(\vec{x})_j \, d\vec{x} = \delta_{ij} \tag{1}$$

$$\vec{v}_k(x, y, t) = \sum_{i=0}^{N} a_{ki}(t)\Phi_i(x, y) \tag{2}$$

where δ_{ij} is the Kronecker delta, L is the integration domain, and Φ is the POD eigenfunction. The $v_k\,(x,y,t)'s$ represent each of the detrended velocity fields in the data set of images. In our case $v_k\,(x,y,t)$ refers to the fluctuation velocity in the horizontal mid-plane of the gap.

The energy contained in each of the POD eigenfunctions can be defined by the spatial mean square value as:

$$E_k = \int_L \|\Phi_k(\vec{x})\|^2 \, d\vec{x} \tag{3}$$

where $\|.\|$ denotes the norm as defined by the usual inner product.

Often the first few functions contain most of the energy. This allows the use of a truncated expansion as an efficient representation of the filtered flow.

The eigenvalues and eigenvectors are determined from the solution of a Fredholm integral of the type:

$$\int_L R(\vec{x}; \vec{x}')\Phi(\vec{x}')d\vec{x}' = \lambda\Phi(\vec{x}) \tag{4}$$

where the kernel is the averaged autocorrelation function $R(\vec{x}; \vec{x}') = (v(\vec{x}), v(\vec{x}'))$. The POD coefficients, a_{ki}, for any realization v_k are extracted by projecting each realization in turn onto the basis set:

$$a_{ki}(t) = \frac{(\vec{v}_k(\vec{x}, t), \Phi_j(\vec{x}))}{(\Phi_i(\vec{x}), \Phi_j(\vec{x}))} \tag{5}$$

E. The Snapshot Method

The method of snapshots developed by Sirovich[6] and employed in this investigation becomes particularly efficient in situations where the number of data realizations is significantly smaller than the number of data points in one particular realization. Sirovich showed that the solution of Eq. (4) is equivalent to the location of the eigenvalues and eigenvectors of a matrix C, whose entries are defined as:

$$C_{m,n} = \frac{1}{N} \int_L v(\vec{x}, t_m)v(\vec{x}, t_n)d\vec{x} \tag{6}$$

The POD eigenfunctions can then be constructed as:

$$\vec{\Phi}_i(\vec{x}) = \sum_{k=1}^{N} \Psi_k^i \vec{v}_k(\vec{x}, t) \tag{7}$$

Where Ψ_k^i is the ith component of the kth eigenvector, $\vec{\Psi}_k$.

In situations where the number of data realizations is N, and the total number of data points in a particular realization is M, use of the snapshot method reduces the problem from the solution for the eigenvalues of a M x M matrix to the that of a N x N system (with N<M).
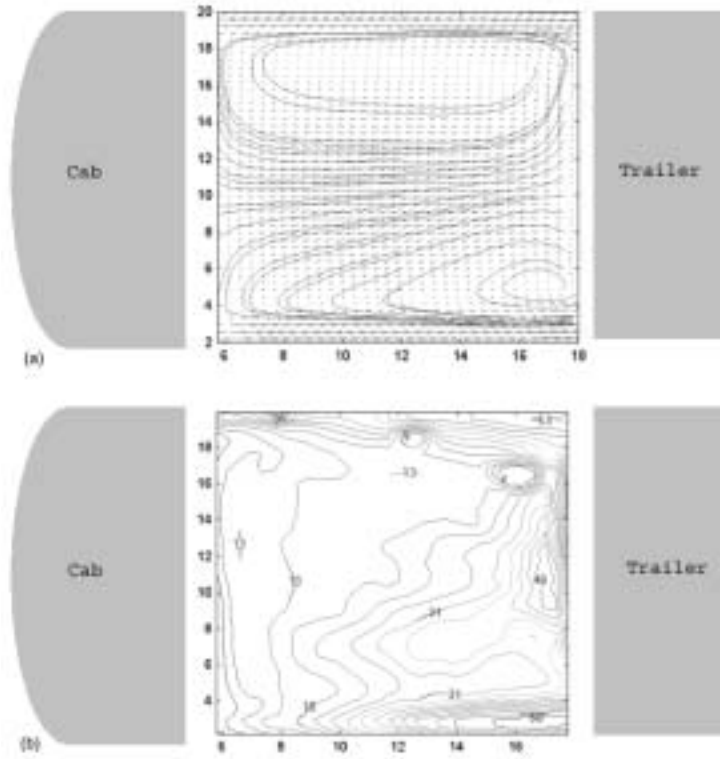
Figure 9. (a) Ensemble average of the velocity field, (b) ensemble average of the fluctuation kinetic energy (m^2/s^2).
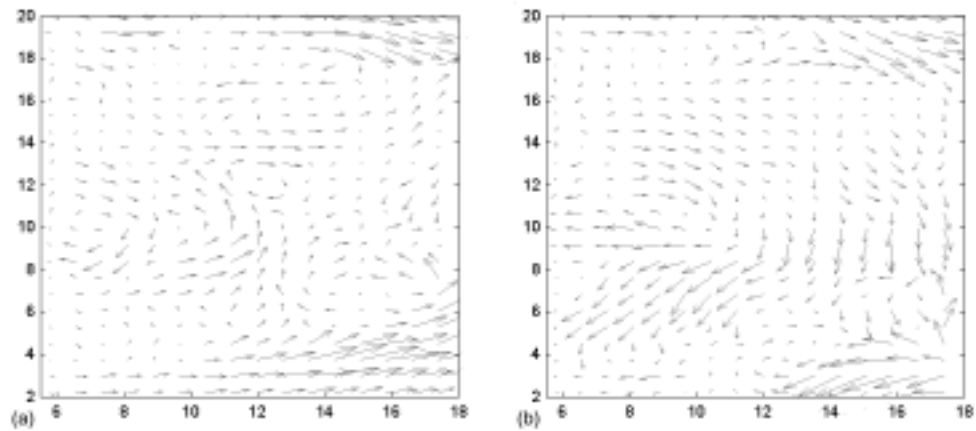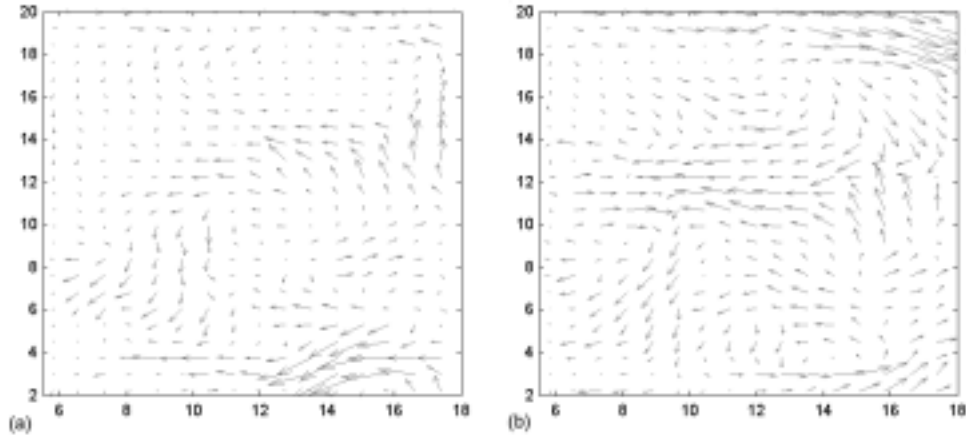

Figure 10.   Fluctuation velocity realizations with simultaneous strong motion in both corners of the trailing body: (a) realization 92, (b) realization 184.

III.   Results

The ensemble average of the 344 velocity fields (snapshots) recorded in the gap and containing good data, at $G/\sqrt{A}=0.72$ and zero yaw is shown in Fig. 9(a). The mean flow pattern is characterized by the presence of two shear layers that bound the gap on either side (top and bottom in the figure). Two counter rotating circulations are positioned upstream of the trailing body, and an extensive area of backflow occupies most the central region of the gap. A slight asymmetry is evident. This is most likely due to a slight experimental uncertainty in the location of the zero yaw angle.

To evaluate the strength of the turbulent motion in the flow, the mean fluctuation kinetic energy of the ensemble as defined by $k=u'^2+v'^2$ has been computed and isocontours of kinetic energy have been represented in Fig. 9(b). The two small regions near (13,18) and at (16,16) are spurious (possibly imperfections on the window). Two regions can be distinguished with markedly different levels of turbulent kinetic energy. One of the regions spans a triangular shaped space occupying roughly half of the gap. This region is shielded from the free stream by the leading body and exhibits low levels of turbulent kinetic energy. A second region of more intense turbulent behavior is located closer to the nose of the trailing body, and within the shear layers bounding the free-stream. The highest levels of turbulent kinetic energy in the domain, are located in the neighborhood of the rounded corners of the trailing body. The small asymmetry observed in the mean field is also present in the mean fluctuation kinetic energy. It is also of interest to notice the existence in the data set of velocity fields in which this strong turbulent motion in the neighborhood of both corners occurs simultaneously as observed in Fig. 10, and fields in which this feature is only present near one of the corners as shown in Fig.11.

Figure 11.   Velocity realizations with strong fluctuating motion in only one corner of the trailing body: (a) realization 69, (b) realization 81.

A. The Proper Orthogonal Decomposition

Further information about the flow is now sought by performing a Proper Orthogonal Decomposition (POD) of the data. The results of POD analysis indicate that fluctuation energy is strongly concentrated in the first few modes, making the POD decomposition an optimal tool for the analysis of the flow. The energy distribution of the first 50 modes as obtained from POD analysis is shown in Fig. 12. It can be observed that the first mode alone accounts for 24.6% of the energy of the fluctuation field, followed by the 2nd, 3rd, 4th and 5th modes with respectively 10.6%, 6.4%, 4.2% and 3.7% of the total energy. Together the first 5 modes account for 49.5% of the turbulent energy.

As depicted by mode 1, flow enters the gap from the right hand side (looking upstream), crosses the gap and exits on the left hand side. Cross-gap velocities are highest near the trailer face. A portion of the crossing flow returns along the base of the cab to supply entrainment for the shear layer separating from the cab on the right hand side. The shear layer separating from the left hand side of the cab has been displaced away from the surface by the strong cross flow, and indicates that separation occurs somewhere upstream of the corner of the cab. The clockwise circulation in the gap is centered in the neighborhood of (8,10).
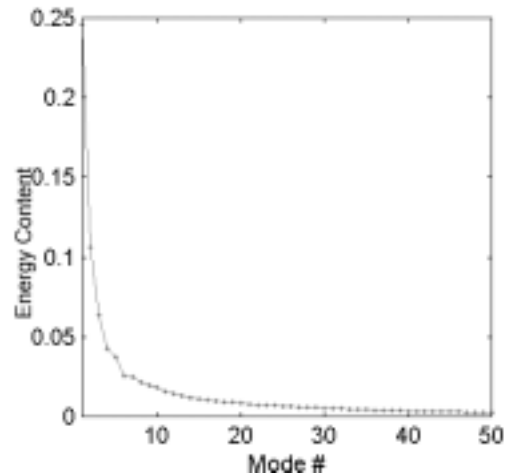
Mode 2, on the contrary, contains a much more symmetric structure (if one disregards small uncertainties in the yaw angle). It is dominated by the presence of two counter rotating circulation regions each one roughly spanning half of the gap space. Both modes 1 and 2 exhibit strong turbulent motion near the rounded corners of the trailing body justifying the high levels of mean turbulent kinetic energy present in that region as noted in Fig 9(b).

Mode 3 also shows a relatively symmetric structure where the flow is being convected from the free stream sides of the gap and redirected towards the wall of the trailing body, however, no strong motion at the corners of the trailing body takes place in this mode.

Mode 4 is clearly asymmetric and shows a structure with flow being convected from one of the free stream sides of the gap to the opposite through a winding path in which the flow is forced to change direction several times before reaching the opposite side of the gap. In this mode, a strong motion is present at the right corner (upper) of the trailing body but not at the left (lower) corner.

Figure 12.   Fractional energy distribution for the first 50 POD modes.
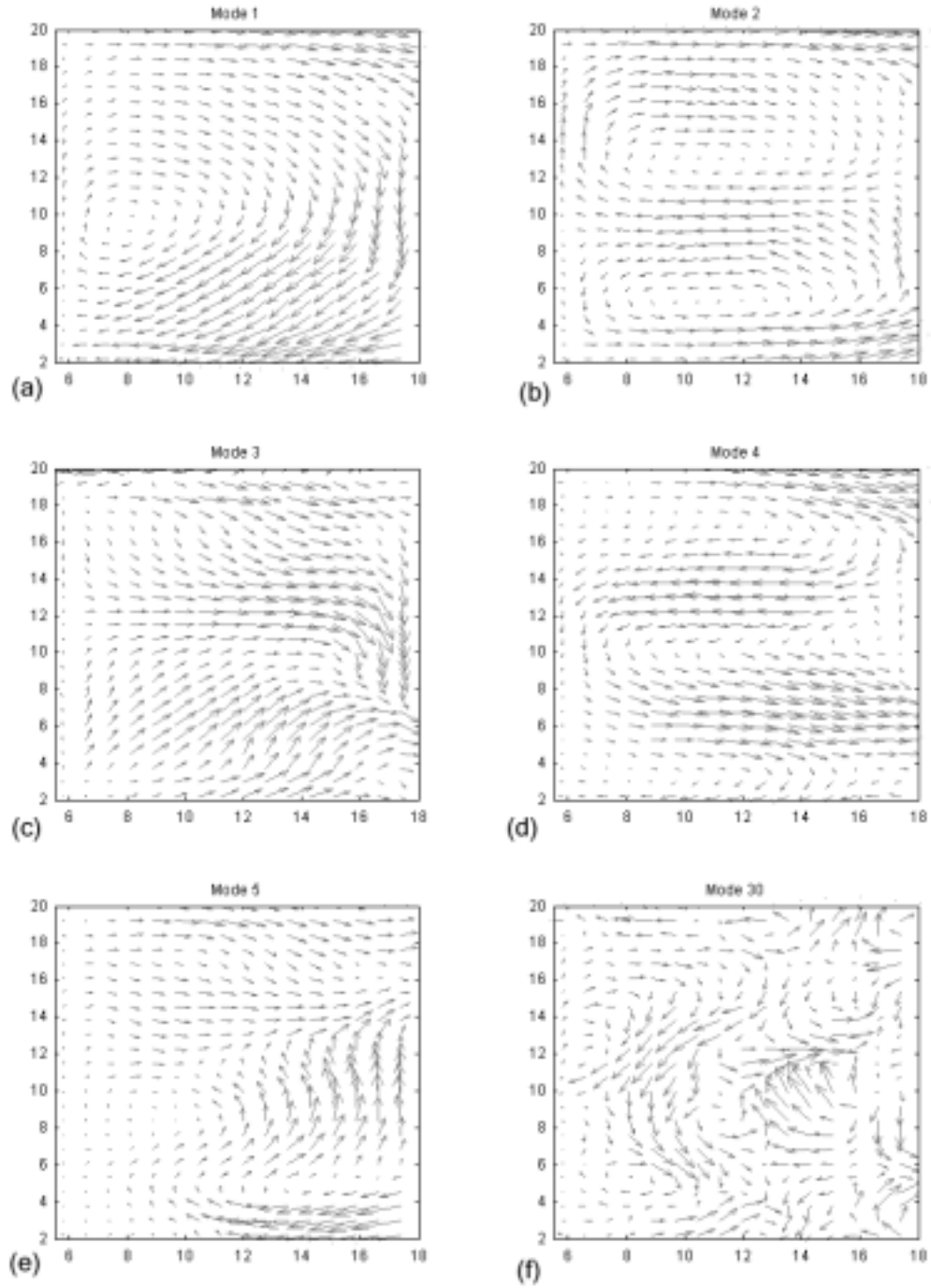
Mode 5 exhibits a somewhat asymmetric structure and as finer details commence to appear in higher modes, symmetry fades away and gives rise to more noisy fields. One interesting feature, however, of mode 5 is the presence once again of strong velocity fluctuations in the left (lower) trailing corner, representative of velocity fields of the type shown in Fig. 11(a).

Mode 30 containing only 0.3% of the energy, is shown in Fig. 13(f) to exhibit the typical finer structure of higher modes having smaller energy content and probably little physical significance.
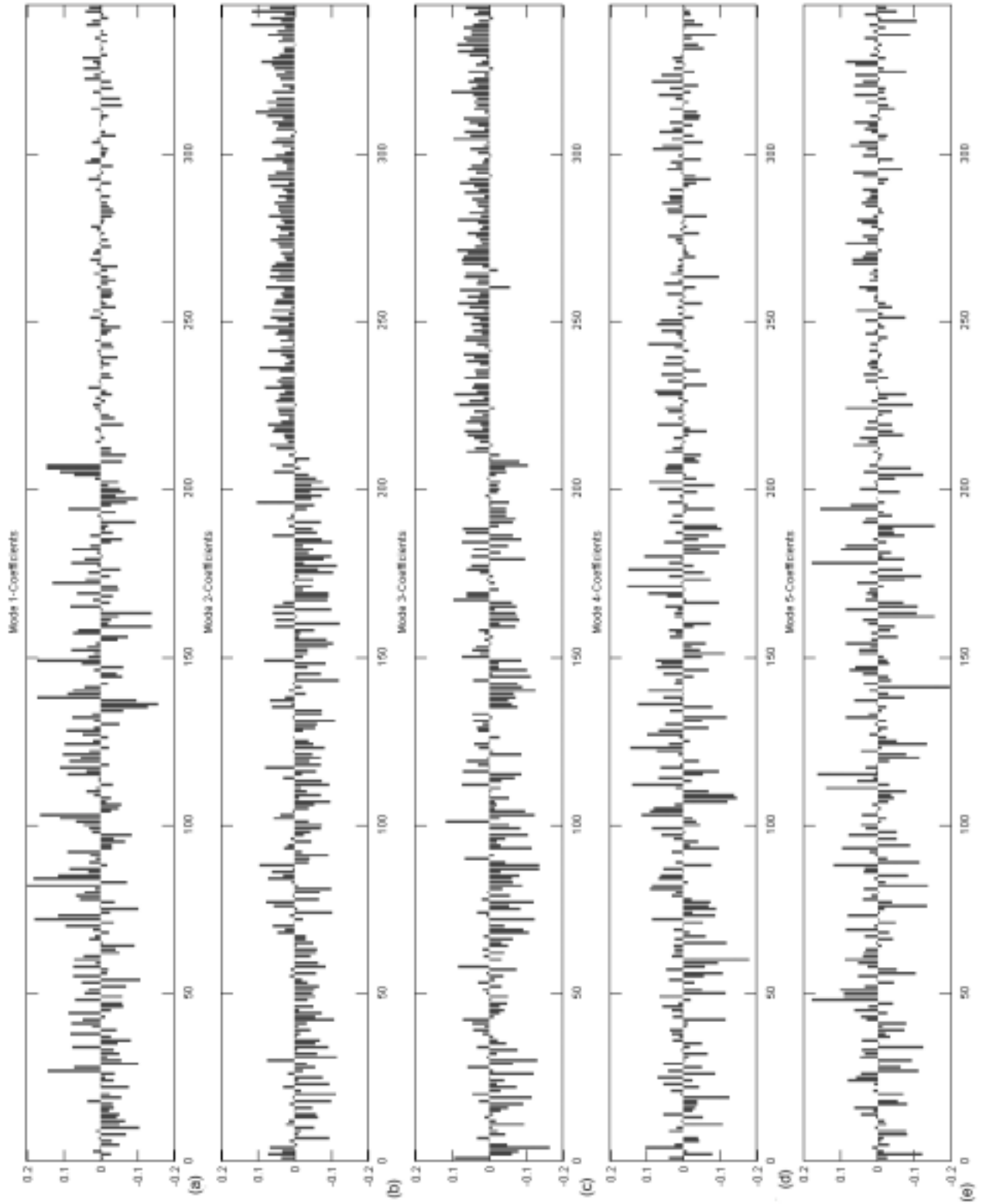
American Institute of Aeronautics and Astronautics

Figure 13.   Structural features of POD modes: (a) 1, (b) 2, (c) 3, (d) 4, (e) 5 and (f) 30.

Figure 14. **POD Coefficients associated with modes: (a) 1, (b) 2, (c) 3, (d) 4 and (e) 5, (data set analyzed in chronological order).**

B. Reconstructing the Time Series from POD Contributions.

Due to the high level of energy concentration in the first few modes and to the fact that the eigenmodes found in POD analysis form an orthogonal basis set optimal (from an energy standpoint) for the description of the data, every velocity realization in the set can be efficiently approximated by a linear combination of the first few more energetic modes. The coefficients $a_{ki}(t)$ (the coordinates in the POD-modes basis set) associated with each of the orthogonal eigenmodes would, consequently, represent the amount of a particular mode present in each velocity realization.

When the contribution of each of the first 5 POD modes to each velocity realization is plotted sequentially as in Fig. 14, an additional and interesting flow feature is revealed by the POD coefficients. The flow convection time, based upon the trailer width $\tau=w/U_o$, is of the order of 0.006 seconds. The low frequency sampling employed in the DPIV (10 Hz.) is not sufficient to resolve time development of the flow field, so the individual realizations in Fig. 14 are a series of snapshots, but not a time series in the usual sense of the word.

However, when coefficients associated with chronologically ordered velocity fields are plotted, two clearly distinct regions emerge in POD-space. The two regions are particularly distinguished in panels (a), (b), and (c) of Fig. 14 showing the contribution of modes 1, 2 and 3. In panel (a), representing coefficients associated with mode 1, the two regions indicate a qualitative change in flow behavior and are characterized by an early-time behavior in which the flow shows evidence of strong and violent contributions of mode 1, endowing the flow with a high energy content. In this regime, changes in the direction of flow across the gap are frequent as reflected in the sign switching of POD coefficients. This early stage of the flow ranges from velocity realization 1 to around realization 211. A later stage with a much smaller contribution from mode 1 extends roughly from velocity realization 211 to 344. The late-time behavior is associated with fields of lower energy content.

The same two regions but with different structural characteristics from those found for mode 1, can easily be distinguished in panels (b) and (c) associated with modes 2 and 3 respectively. The information contained in these two panels reveals that the contribution of modes 2 and 3 to velocity realizations associated with the high energy phase is dominated by negative coefficients, contributing a velocity distribution similar to that depicted in the representation of modes 2 and 3 in Fig. 13, but with opposite direction. A more moderate and positive contribution of modes 2 and 3 to the low energy stage (realizations 211-340) can also be inferred from panels (b) and (c). The fact that the presence of these two regions becomes evident when coefficients are ordered in a chronological manner along the abscissa, points to the existence of a longer time scale in the flow, a time scale of sufficient duration to be resolved by the low sampling frequency employed of 10 Hz. Failure to record a smooth continuous signal within each of the two regions is, nonetheless, a clear indication of the existence of much shorter time scales in the flow that are not resolved at the current sampling frequency.

C. An Alternative Classification

The unexpected identification of strong flow asymmetries, and the implications this phenomenon may have on aerodynamic drag and lateral stability properties of the vehicle served, as motivation to pursue a more detailed analysis. A somewhat ad hoc method of classifying and quantifying the degree of asymmetry in each velocity field was developed. The gap space was divided into two halves, as shown on Fig. 15. The spatial average of the cross-gap velocity was then computed in each half of the gap and labeled v1 and v2 respectively. The two dimensional space spanned by each pair (v1$_i$,v2$_i$) associated with the ith velocity realization provide a qualitative description of the symmetry or asymmetry of the flow. When the coordinates of a particular realization fall close to the origin, the flow may be judged to be symmetric about the longitudinal vertical mid-plane. Further more, the flow in each half space has near zero mean. When the state-space coordinates v1 and v2 are positive, an asymmetric state is present in the flow with fluid being convected from left hand side to right hand side. When the v1 and v2 are negative the flow is asymmetric, but in the opposite sense. The application of these criteria to the data set, as in Fig. 16, reveals that all three possible situations (1 symmetric plus 2 asymmetric) are present in the gap flow at
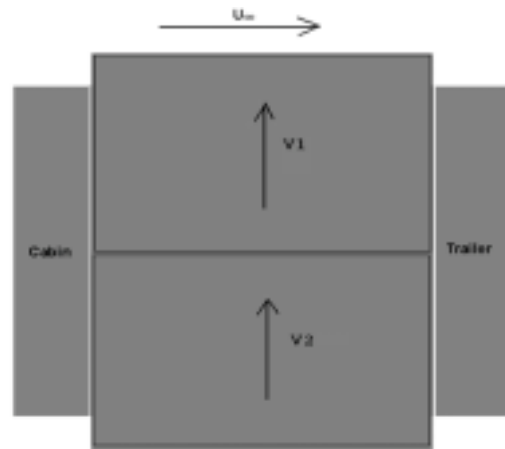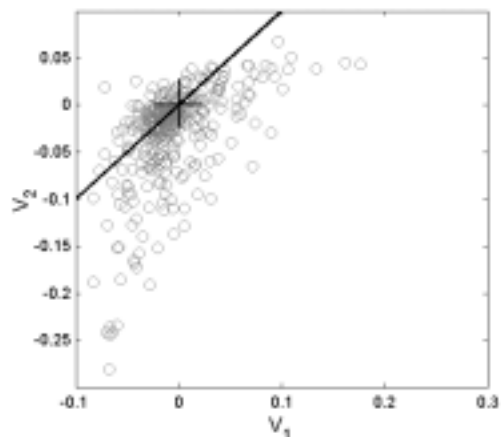

Figure 15.   Definition of state-space variables v1 and v2.

zero yaw. The state space is populated along a crescent-(or croissant-shaped) region. The center of the croissant lies near the origin and the two arms extend horizontally and vertically. The shape is such that large positive values of v1 are associated with positive but modest values of v2. The opposite leg is associated with large negative values of v2 and modest negative values of v1. The croissant is not perfectly symmetric in the sense that the negative arm appears stronger than the positive arm. The larger excursions occurring in the negative arm are a reflection of some slight model yaw or other asymmetry in the model arrangement.
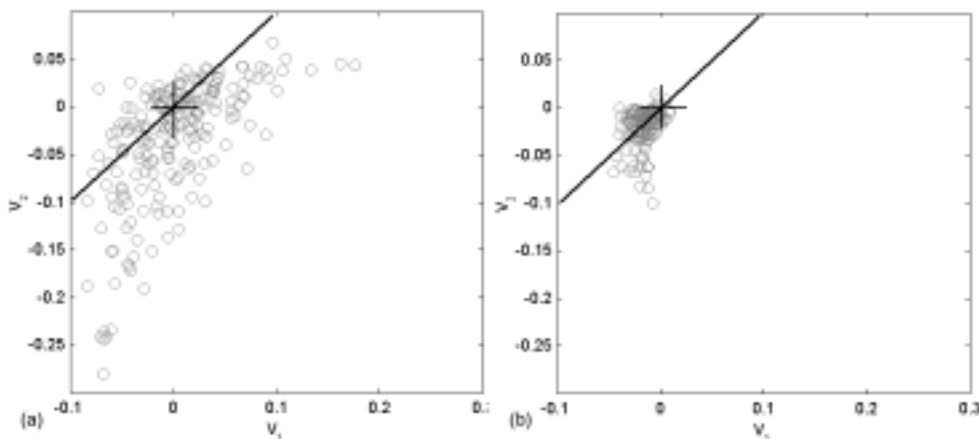
We can now ask where the "high" and "low" energy regimes discovered in Fig. 14 lie on the state space map. Fig. 17 shows the state-space distribution of velocity realizations belonging to (a) the high-energy stage, and (b) the low energy stage. It becomes evident in Fig. 17 that the high-energy phase consists of all three states, with the flow transitioning from one highly asymmetric state to the opposite state through an intermediate symmetric state and with state-space coordinates spanning the entire croissant-shape.

Figure 16.   State-space distribution for the mid-plane of the gap (Gap=0.72).

The velocity fields associated with the low energy region, however, exhibit a population distribution centered about the origin with very moderate excursions into the asymmetric regions, confirming the presence of predominantly symmetric velocity fields. On the basis of the evidence obtained to this point we can surmise that the flow in the mid-plane of the gap presents at times, a high energy phase with highly asymmetric velocity fields and at other times a second phase with mainly symmetric velocity fields and a much more moderate energy content.

To further investigate the flow, a second presentation of POD coefficients associated with modes 1, 2, 3, 4 and 5
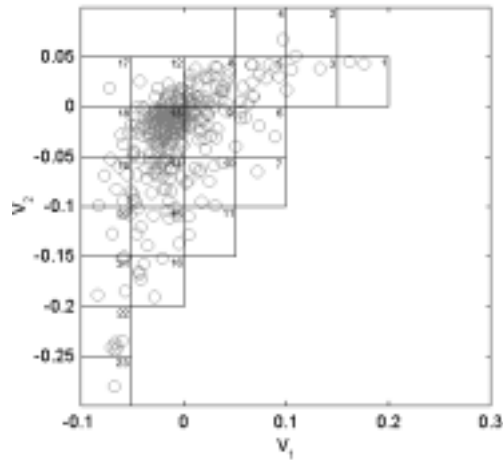

Figure 17.   Distribution in state-space of realizations: (a) 1 through 211 (high energy) and (b) 212 through 344 (low energy).

was employed. A new ordering scheme based on the results of state-space analysis was devised as follows. The croissant-shaped space in the (v1,v2)-plane was divided into 23 rectangular regions, each containing a number of state-space points associated with several of the velocity realizations. Each one of the regions was numbered as shown on Fig. 18. The idea was to traverse the croissant-shaped space starting from the end of one the arms and ending at the end of the opposite arm, effectively transitioning from velocity realizations with one asymmetric state, through symmetric realizations, to realizations with opposite asymmetry. The solution to the numbering and location of each one of the rectangular regions is not unique since there is some ambiguity as to the most suitable way to transition from one rectangular region to another. Nonetheless any of the solutions should be appropriate to render a set of velocity realizations having the intended trend in a general sense. It is also important to notice that different velocity fields associated with the same rectangular division will maintain the original chronological order. The result of presenting the graphs of Fig. 14 according to the new ordering of the abscissa is shown in Fig. 19. Figure

Figure 18.   Distribution and ordering of the 23 rectangular divisions in state-space.

19 (a) reveals the effect of mode 1 on the asymmetric states of the flow and it shows that the amount of mode 1 present in each velocity field controls the level of asymmetry in the flow, while other asymmetric modes contribute much more lightly to the generation of asymmetric fields. When velocity fields are analyzed in order of increasing levels of asymmetry as described by state-space analysis, a relatively smooth, clear and increasing trend appears in the POD coefficients of the first mode. The presence of a velocity field on either leg of the croissant-shaped space will be determined by the sign of the coefficient associated with mode 1, and as one transitions from one leg to the other one traverses a region of symmetric velocity fields close to the origin with almost vanishing contributions of mode 1. This establishes the connection of mode 1 with the asymmetric states of the flow residing far away from the origin in state space and having a high energy content.

Further information can be extracted from the contributions of modes 2 and 3. In the bar plots of Fig. 19 it is particularly striking to observe the change in trend of a subset of realizations within one rectangular division, for instance in the contribution of mode 2 to quasi-symmetric velocity realizations associated with rectangular region 13, and ranging from realization 131 to realization 271 (according to Fig. 19). A distinct subset with different trend than the rest of the members of the set is clearly identified in realizations 131 through 166. The difference in trend is not only observed in mode 2, but persists also into modes 1, 3, 4 and to a lesser extent into mode 5.
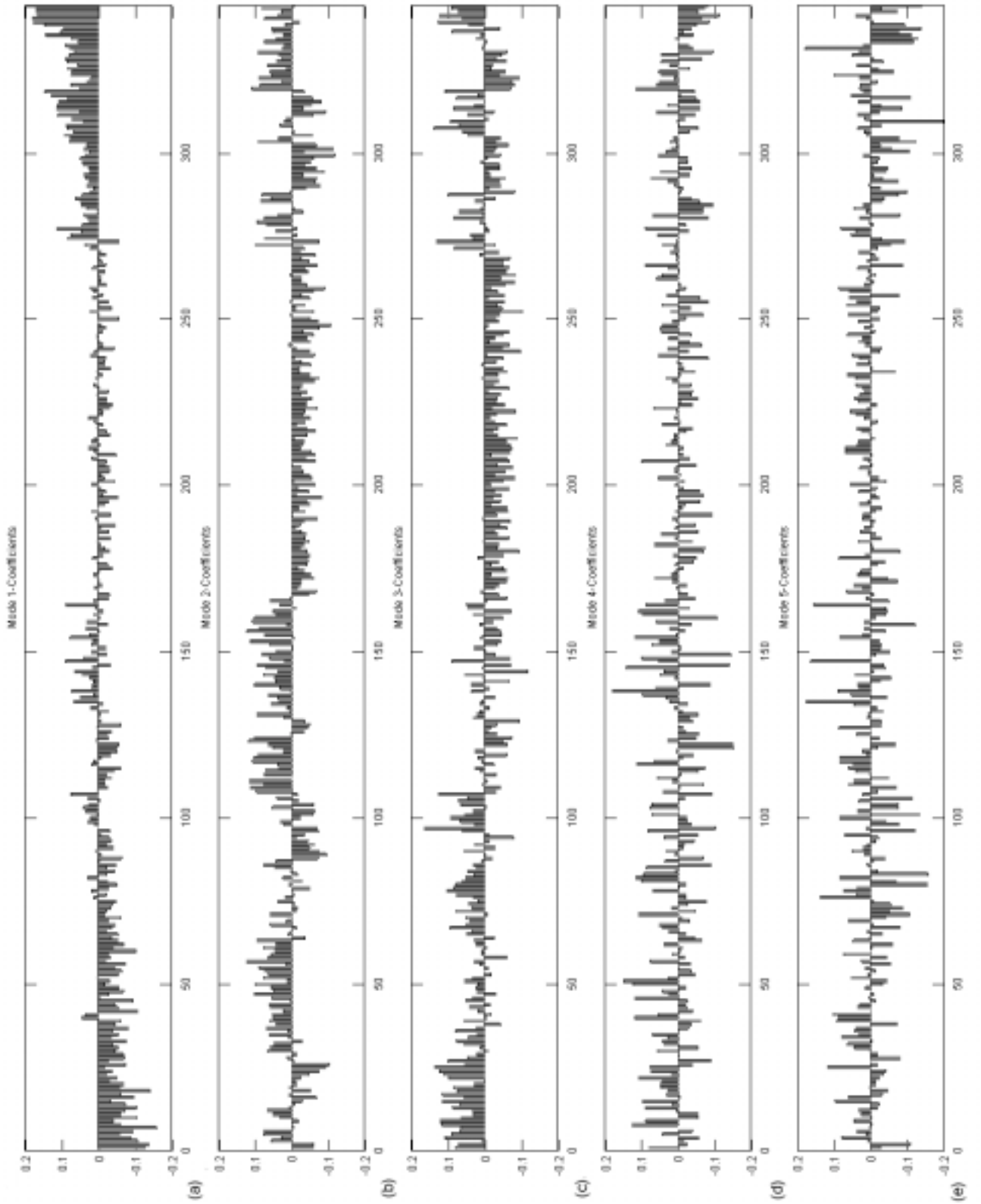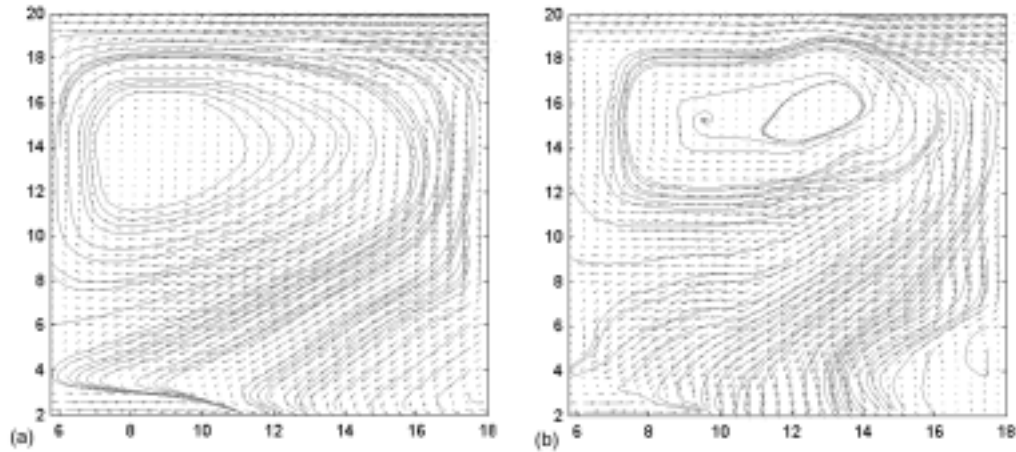
The same phenomenon may be observed in other sets associated with other state space divisions, for instance, in the set formed by realizations 272 through 302 (according to Fig. 19) and associated with rectangular region 14, the subset of realizations 272 through 287 exhibits clearly different features from those of other members of the set, and the same is true for the set made up of realizations 108 through 130 associated with region 11 and with a well-defined subset in realizations 106 through 124. The differential structural composition of subsets of realizations which otherwise share the same symmetric structure is indicative of the existence of additional structural features not captured by state space analysis, and that only emerge after a POD decomposition of the flow is performed.

The reason for the differential structural composition between realizations belonging to the same region in state-space is found by tracking down the origin of each realization present in Fig. 19. Once this has been done, it becomes evident that even though every realization in the central region of Fig. 19 exhibits a symmetric or quasi-symmetric state, subsets of fields 106 through 124, 131 through 166 and 272 through 287 (according to Fig. 19) correspond to symmetric velocity distributions with high energy content that occurred during the early high energy phase of the flow. They probably represent transitional stages between two high energy asymmetric states, whereas the rest of the members of their respective sets are associated with symmetric or quasi-symmetric velocity fields originally associated with the later-time low energy phase into which the flow seems to settle. The lumping together of *transitional* or *steady* state realizations within one particular rectangular region in state space can be explained in terms of the ordering scheme employed. Even though in general, all the realizations in the data set have been ordered on the basis of their location in state space, locations within the same rectangular retain their original chronological order. Therefore, within the same rectangular division, *transitional* velocity fields that occur earlier in the flow are lumped together to the left of *steady* state fields that occur at a later time, establishing a new temporal subdivision within the spatial divisions of state space. On the basis of these findings we can establish the existence of a different modal composition for *transitional* symmetric states and for *steady* state symmetric states.

To obtain a visual interpretation of the flow structure in each of the possible states, namely asymmetric with strong lateral transfer right to left, asymmetric with transfer left to right, *transitional* symmetric and *steady* symmetric, a representative member of each one of the asymmetric states was selected and reconstructed using only the first 2 POD modes and superimposing the result on the mean flow. The use of only a reduced number of the most energetic modes in the description of the flow will render filtered velocity fields in which the main organized structures of the flow will emerge while finer details will be suppressed. Fig. 20 represents (b) an unfiltered, highly asymmetric velocity field with flow from left to right and (a) shows the filtered field associated with the velocity field of panel (b). It becomes evident in panel (a) that the flow is characterized by the presence of a center of counter clockwise circulation centered in the neighborhood of (8,7), and driven by an input of energy from the left side shear
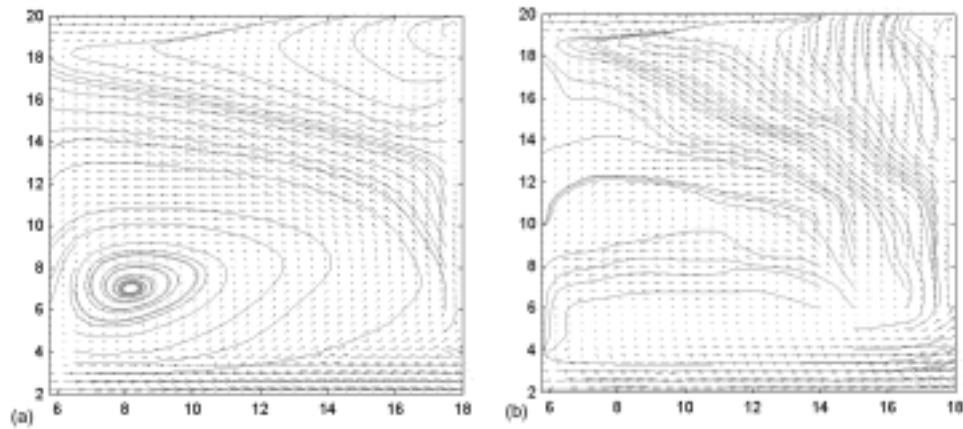
Figure 19. POD Coefficients associated with modes: (a) 1, (b) 2, (c) 3, (d) 4 and (e) 5, (data set analyzed in order provided by state-space analysis).

Figure 20. **(a) Filtered asymmetric state with flow across gap from left to right; (b) unfiltered asymmetric state in (a).**


Figure 21. **(a) Filtered asymmetric state with flow across gap from right to left; (b) unfiltered asymmetric state in (a).**

layer. The vortex organizes the flow in the entire region and establishes a strong backflow in the gap with fluid leaving the domain by entrainment into the top shear layer. When a representative member of the opposite asymmetric state is analyzed using the same procedure, the same structural organization is revealed although the location of the center of the vortex is positioned in this case around (8,14) and its rotation is in the clockwise direction as shown in Fig. 21 where two images, for the unfiltered (b) and filtered velocity fields (a) are again displayed. Due to the absence of a well-defined trend in the coefficients of the symmetric realizations, two average velocity fields representative of each of the two subsets in the symmetric cases (*transitional* and *steady*) were constructed using the first 2 orthogonal modes and compared with each other. The visual identification of the structural composition of the symmetric states of the flow proved to be more complicated in this case. Differences between the *transitional* and the *steady* symmetric states are not obvious from examination of the filtered velocity fields of Fig. 22. Both contain two counter-rotating circulations, and a large area of backflow in the center of the gap. No substantial differences between the two subsets can be readily identified.

Differences, however, start to surface as one examines the (unfiltered) average vorticity fields representative of each subset. A substantial difference in the negative vorticity intensity of the right side (top side of the picture) shear layer of almost 50% becomes evident in Fig. 23. The reason for the differential vorticity distribution can be understood after a close examination of the filtered fluctuation (detrended) velocity fields, represented in Fig. 24. The two are characterized by the presence of two counter-rotating centers of circulation positioned in a relatively
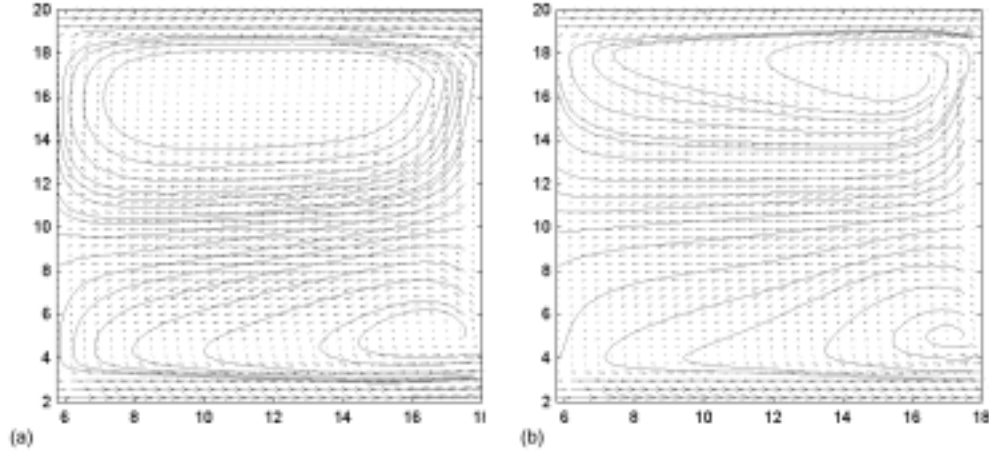
Figure 22. Filtered average velocity field: (a) realizations 131 through 166 (*transitional*), (b) 167 through 271 (*steady*).
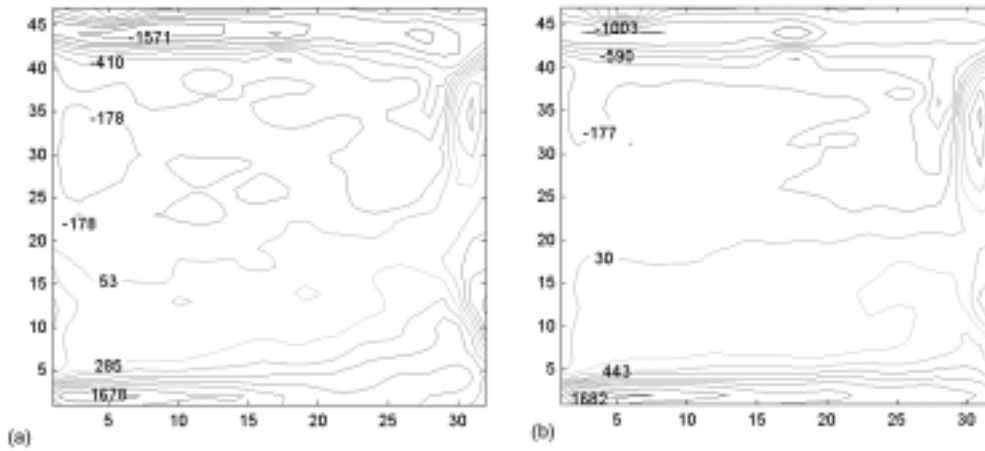

Figure 23. Unfiltered average vorticity field (s⁻¹): (a) realizations 131 through 166 (*transitional*), (b) 167 through 271 (*steady*).

symmetrical manner about the longitudinal vertical mid-plane. The direction of rotation of the two-vortex system, however, is opposite for fields associated with the *transitional* and the *steady* symmetric states. In the case of *transitional* symmetric states (panel (a)), the fluctuation vortex circulation adds to the free stream velocity of the upper shear layer, increasing the velocity gradient and generating higher levels of negative vorticity. In the case of *steady* symmetric states, the vortex rotation is opposite and it reduces the amount of shear as one transitions from the core of the upper vortex into the free stream on the right side, effectively reducing the velocity gradient and resulting in lower levels of negative vorticity. The direction of circulation of the fluctuation velocity resulting in the different vorticity distribution between the *transitional* and the *steady* symmetric states can also be interpreted in terms of the POD modal composition of each state. The average velocity fields of Fig. 24 were constructed by computing the average modal contribution of the 1st and 2nd modes to velocity realizations 131 through 166 (according to Fig. 19) (*transitional*) and 167 through 271 (*steady*) and then using modes 1 and 2 to obtain a representative average velocity field. The average modal contributions of the 1st and 2nd modes to *transitional* velocity fields exhibit positive contributions with average values of 0.0184 and 0.0509 respectively, whereas the contributions of the first 2 modes to *steady* states show negative average contributions of -0.0095 and -0.0393 for the first and second modes. The opposite sign of the modal contribution of the first two modes to *transitional* and *steady* symmetric states results in a

reversed direction of circulation in the fluctuation velocity fields of Fig. 24 and is directly responsible for the observed differences in the vorticity fields of *transitional* and *steady* symmetric states.
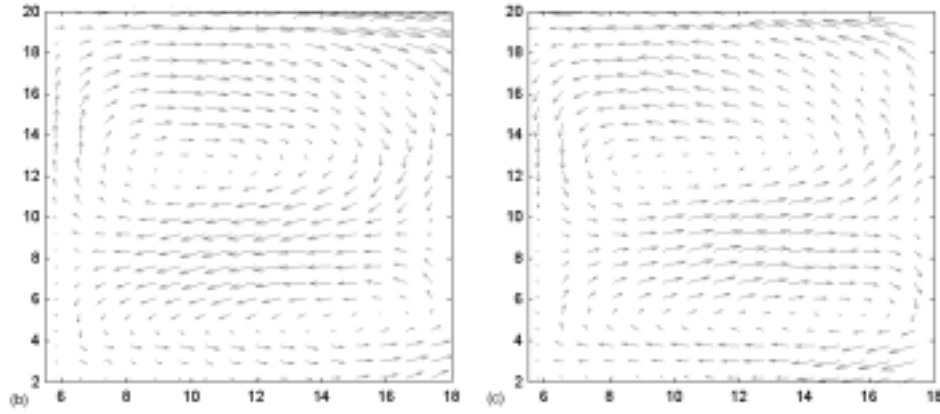
Figure 24.   Filtered average velocity fluctuation fields: (a) realizations 131 through 166 (*transitional*), (b) 167 through 271 (*steady*).

IV.   Conclusions

The flow within the gap exhibits two clearly distinct flow behaviors. At certain times the flow is observed to be dominated by velocity fields exhibiting a high level of symmetry. The flow in this stage is organized into two nearly symmetric recirculation regions with limited amount of fluid transfer across the gap. Velocity fields associated with this regime of flow tend to exhibit low levels of turbulent kinetic energy.

At other times, the flow is characterized by the appearance of a cross-gap flow structure revealed by both the state-space and the POD analysis. Velocity fields associated with this stage can be identified by the presence of only one of the recirculation regions detected in symmetric fields. A strong asymmetry is induced in the velocity field within the gap, resulting in high levels of fluid transfer in the cross-stream direction. The injection of energetic shear layer turbulence increases the intensity within the gap.

The existence of highly energetic asymmetric fields with strong lateral fluid transfer is less intuitive than that of symmetric fields. POD analysis reveals that the asymmetric fields exhibit a particular modal composition dominated by the presence of a very energetic asymmetric lowest mode structure. This lowest mode is absent when the flow field is symmetric.

Asymmetric velocity fields alternate between two possible solutions, one with fluid transfer from top to bottom of the gap and the opposite with fluid transfer from bottom to top. The transition from one situation to the opposite takes place by means of *transitional* symmetric velocity fields apparently similar to *steady* symmetric realizations, but with structural differences that surface only after a detailed examination of the vorticity and filtered velocity fluctuation fields. Higher vorticity in the right side shear layer is associated with *transitional* symmetric states, and lower values of vorticity are associated with *steady* symmetric ones. *Transitional* symmetric states appear as migrating dots located around the origin in the state-space of Fig. 16. They travel from one of the arms of the 'croissant' to the opposite arm while *steady* symmetric states lie in the neighborhood of the origin and stay there for longer times.

Referring again to Fig. 1, we can now offer an explanation for the rapid rise in drag associated with increasing gap length in the range G/√A=0.5-0.7. The drag increase occurs precisely at the onset of strong cross-gap flow as observed by the state space analysis and in more detail by the Proper Orthogonal Decomposition. The cross-gap flow is strong enough in magnitude to effect boundary layer separation forward of the base of the cab on the outflow side, and to greatly increase the momentum deficit on this side. The increased momentum deficit results in increased drag.

For gap separations in the interval G/√A=0.7-1.1, the effect of the cross-gap flow gradually subsides because the gap is larger and the cross-gap flow velocity is diminished. The drag decreases slightly from the largest value at G/√A=0.7. Beyond G/√A=1.1, the mean cab wake has closed, exposing the trailer to larger oncoming flow

velocities, and the drag begins to rise again, but now more slowly on a scale commensurate with the length scale required for velocity recovery in the turbulent wake.

References

[1]Cooper, K., "The Effect of Front-Edge Rounding and Rear-Edge Shaping on the Aerodynamic Drag of Bluff Vehicles in Ground Proximity," *SAE-SP 850288,*February, 1985.

[2]Fincham, A. M., Spedding, G. R., "Low Cost, High Resolution DPIV for Measurement of Turbulent Fluid Flow," *Experiments in Fluids*, Vol. 23, 1997.

[3]Hammache, M., Browand, F. K., "On the Aerodynamics of Tractor-Trailers," (to be published in) *Proceedings of the UEF Conference on The Aerodynamics of Heavy Vehicles: Trucks, Buses and Trains*, Heidelberg, Springer-Verlag.

[4]Koenig, K., Roshko, A., "An Experimental Study of Geometrical Effects on the Drag and Flow Field Around Two Bluff Bodies Separated by a Gap," *Journal of Fluid Mechanics*, Vol. 156, 1985, pp. 167, 204.

[5]Lumley, J. L., *Stochastic Tools in Turbulence*, Academic Press, New York, 1970.

[6]Sirovich, L., "Turbulence and the Dynamics of Coherent Structures. Part 1: Coherent Structures ," *Quarterly of Applied Mathematics*, Vol. XLV, No. 3, 1987, pp. 561, 571.